APPLIED SCIENCES AND ENGINEERING

Magnetic-actuated "capillary container" for versatile three-dimensional fluid interface manipulation

Yiyuan Zhang[1], Zhandong Huang[1]*, Zheren Cai[2,3], Yuqing Ye[4], Zheng Li[2,3], Feifei Qin[5], Junfeng Xiao[1], Dongxing Zhang[6], Qiuquan Guo[6], Yanlin Song[2], Jun Yang[1]*

Fluid interfaces are omnipresent in nature. Engineering the fluid interface is essential to study interfacial processes for basic research and industrial applications. However, it remains challenging to precisely control the fluid interface because of its fluidity and instability. Here, we proposed a magnetic-actuated "capillary container" to realize three-dimensional (3D) fluid interface creation and programmable dynamic manipulation. By wettability modification, 3D fluid interfaces with predesigned sizes and geometries can be constructed in air, water, and oils. Multiple motion modes were realized by adjusting the container's structure and magnetic field. Besides, we demonstrated its feasibility in various fluids by performing selective fluid collection and chemical reaction manipulations. The container can also be encapsulated with an interfacial gelation reaction. Using this process, diverse free-standing 3D membranes were produced, and the dynamic release of riboflavin (vitamin B_2) was studied. This versatile capillary container will provide a promising platform for open microfluidics, interfacial chemistry, and biomedical engineering.

INTRODUCTION

Fluid interfaces, including gas-liquid interfaces and liquid-liquid interfaces, are ubiquitous in nature and widely used in industrial applications. They can be water droplets in air, gas bubbles underwater, oil-water emulsions, soap foams, etc. The sudden change of physical parameters across the fluid interface triggers many fundamental interfacial processes, such as diffusion, reaction, adsorption, instability, evaporation, self-assembly, and acoustic resonance. These processes form the pivot of chemistry, physics, biology, and material science. For instance, evaporation is an essential driving force for water cycle (*1*), energy conversion (*2*, *3*), high-resolution printing (*4*, *5*), and surface patterning (*6*). Acoustic resonance of bubbles is broadly used in ultrasound imaging (*7*, *8*), acoustic tweezers (*9*, *10*), and metamaterials (*11*, *12*). The interfacial reaction and diffusion form the basis of chemical synthesis (*13*, *14*), drug release (*15*), extraction (*16*), and separation (*17*, *18*). Adsorption benefits water treatment (*19*), froth flotation (*20*), and food processing (*21*). Fingering instability plays a vital role in oil recovery and hydrology (*22*, *23*). Meanwhile, the "soft" fluid interface offers a powerful platform for self-assembly (*24*, *25*). Engineering the fluid interface in a flexible manner can be very attractive for interfacial process research and technological renovations. However, owing to the interfacial instability and fluidity, precise control of fluid interface remains a great challenge, especially for creating the three-dimensional (3D) stable fluid interfaces and their programmable dynamic manipulation.

To date, most studies are based on microfluidics (*26*) to create controlled fluid interfaces, which are limited to simple emulsion droplets, floating bubbles, and planar pinned interfaces (*27*). To create complex fluid interfaces, many efforts have been made. For example, complex 2D gas-liquid interfaces have been generated by regulating the 2D liquid foam evolution for functional material assembly (*28*). The multimaterial fluid interface patterning has been realized by using microstructures with predefined wettability for microdevice fabrication (*29*). These methods can stabilize the 2D fluid interfaces, but they disable the mobility of the interfaces. To enable dynamic manipulation, electric (*30*, *31*), acoustic (*32*, *33*), and magnetic fields (*34*–*36*) were used to actuate the fluid interface's motion. However, they are only applicable in the manipulation of droplets or bubbles. Therefore, complex 3D fluid interface creation and its dynamic manipulation have never been achieved.

Here, we proposed a magnetic-actuated "capillary container" to realize the stable 3D fluid interface construction and programmable dynamic manipulation for various applications. The capillary container is composed of steel microbeads and a solid frame. With proper wettability modification, the container can trap one fluid in another immiscible fluid to prepare 3D fluid interfaces with different sizes and geometries. Changes in steel microbead distribution and magnet movement alter the degrees of freedom of the container movement. Thus, diverse motion modes including flipping, rotation, and translation are achieved. Moreover, the versatility and universal applicability of the container have been verified in various fluids, with the applications of selective fluid collection and chemical reaction manipulation. Using an interfacial gelation reaction, liquid packaging can be realized with the container. On the basis of this process, various 3D membranes were prepared, and the dynamic release process of riboflavin across the membranes at different pH was studied. This capillary container allows stable 3D fluid interface creation and versatile automated manipulation, opening promising avenues for bubble metamaterials, open microfluidics, interfacial chemistry, and programmable drug delivery and release.

[1]Department of Mechanical and Materials Engineering, University of Western Ontario, London, Ontario N6A 5B9, Canada. [2]Key Laboratory of Green Printing, Institute of Chemistry, Chinese Academy of Sciences (ICCAS), Beijing Engineering Research Center of Nanomaterials for Green Printing Technology, Beijing National Laboratory for Molecular Sciences (BNLMS), Beijing 100190, P. R. China. [3]University of Chinese Academy of Sciences, Beijing 100049, P. R. China. [4]School of Biomedical Engineering, University of Western Ontario, London, Ontario N6A 5B9, Canada. [5]Chair of Building Physics, Department of Mechanical and Process Engineering, ETH Zürich (Swiss Federal Institute of Technology in Zürich), Zürich 8092, Switzerland. [6]Shenzhen Institute for Advanced Study, University of Electronic Science and Technology of China, Shenzhen 518000, P. R. China.
*Corresponding author. Email: huangzhandong@iccas.ac.cn (Z.H.); jyang@eng.uwo.ca (J.Y.)

RESULTS

The basic principle of 3D fluid interface creation

The magnetic-actuated capillary container is composed of steel microbeads and a printed frame. The structured 3D fluid interface is created when fluid 1 is captured by the container in immiscible fluid 2 (Fig. 1A). The solid frame provides the capillary force to trap and pin fluid 1, and the steel microbeads endow the container with mobility under the control of a magnetic field. The structure of the container including the distribution of the steel microbeads and the size and geometry of the frame can be flexibly adjusted. Taking the cube container as an example, the basic principle of 3D fluid interface creation is elaborated (Fig. 1, B to E). In the beginning, the container is fully immersed in fluid 1. When it moves from fluid 1 to fluid 2, two distinct results will be obtained: Fluid 1 is replaced (Fig. 1B) or captured (Fig. 1C). The fluid capture occurs when the container has a stronger affinity for fluid 1 than for fluid 2, or conversely, the fluid replacement takes place. From the perspective of energy, to capture fluid 1, the process in Fig. 1C should be energetically more favorable than that in Fig. 1B, namely, $E_3 < E_2$, where E_2 and E_3 are interfacial energy for the fluid replacement and fluid capture, respectively. The above equation can be converted into (section S1)

$$S_{12} - S_{13}\cos\theta_{123} < 0 \quad (1)$$

where θ_{123} is the contact angle of fluid 1 on the frame (solid 3) in fluid 2 (Fig. 1D). S_{12} is the area of the created fluid interface, and S_{13} is the contact area of fluid 1 and solid 3 (Fig. 1E). Equation 1 indicates that $\cos\theta_{123} > 0$ because S_{12} and S_{13} are positive, namely, $\theta_{123} < 90°$. It demonstrates that the frame should be fluid 1 philic in fluid 2. Meanwhile, given that the total surface area of the solid frame is S_s, $S_{12} < S_{13} \leq S_s$ can be derived because $\cos\theta_{123} \leq 1$. This reveals that the created fluid interface area should be less than the frame's total surface area. Therefore, Eq. 1 suggests that the wettability and geometry of the container are two key factors for the 3D fluid interface creation. Most immiscible fluids serving as fluid 1 or fluid 2 can be categorized as gas, water, and organic solvents (oils). Here, we use air, water, silicone oil, and ethylene glycol (EG) to represent them. We denote fluid 1 is captured by the container in fluid 2 as "fluid 1 in fluid 2." By proper wettability modification to keep $\theta_{123} < 90°$ (table S1), eight kinds of 3D fluid interfaces are prepared. They are water in air, air in water, water in oil, oil in water, EG in air, air in EG, EG in oil, and oil in EG, numbered from 1 to 8 in Fig. 1F. The detailed preparation processes are displayed in movie S1.

Detailed design principles of the capillary container

Next, the cube container is taken as an example to demonstrate the detailed design principle for flexible 3D fluid interface creation and manipulation. Assuming that the cube frame has a length of *a*, the

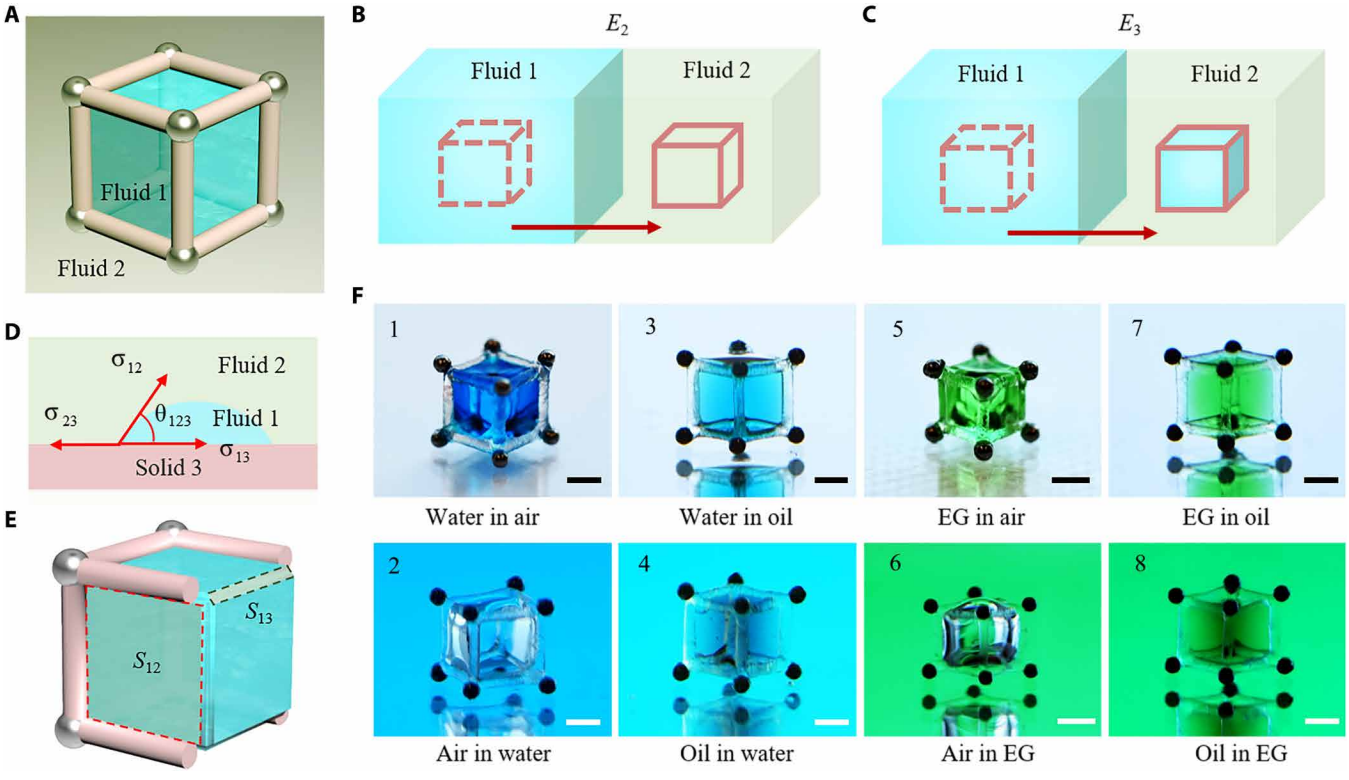

Fig. 1. Schematic illustration of the 3D capillary container and basic principle for 3D interface creation. (**A**) The 3D capillary container consists of printed solid frame and steel microbeads. Fluid 1 and fluid 2 are immiscible fluid pairs composed of water, gas, and organic solvents (oils). (**B** and **C**) Fluid replacement (B) and capture (C) after the container moving from fluid 1 to fluid 2, which has the interfacial free energy of E_2 and E_3, respectively. (**D**) Contact angle (θ_{123}) of fluid 1 on solid 3 (solid frame) in fluid 2. σ_{12}, σ_{13}, and σ_{23} are interfacial tensions of fluid 1–fluid 2, fluid 1–solid 3, and fluid 2–solid 3, respectively. (**E**) Scheme of the created interface between fluid 1 and fluid 2 (S_{12}, marked with the red box) and the contact area between fluid 1 and solid 3 (S_{13}, marked with the gray box). (**F**) Images of the prepared eight kinds of immiscible fluid interfaces, which are numbered from 1 to 8. For distinction, water is colored with blue edible dye, EG is colored with green edible dye, and the silicone oil is colored with Sudan III. Scale bars, 1 mm. Photo credits: Yiyuan Zhang, University of Western Ontario.

edges are cylinders with a radius of r, and $a > 2r$ (Fig. 2, A and B). First, the capillary force should dominate the process in Fig. 1C, namely, the scale of the free fluid interface created by the cube frame ($a - 2r$) must be within the capillary length (*37*, *38*)

$$a - 2r < \sqrt{\sigma_{12}/\Delta\rho_{12}\, g} \tag{2}$$

where σ_{12} is the interfacial tension of fluid 1 and fluid 2, $\Delta\rho_{12}$ is the density difference between fluid 1 and fluid 2, and g is the acceleration of gravity. Here, $(a - 2r)$ is treated as the characteristic length of the 3D fluid interface because it is in good agreement with the experimental results. Second, the magnetic force (F_M) should overcome the maximum resistance during the interface formation process (Fig. 2C). Here, the friction resistance (F_f) is negligible owing to the small friction coefficient between microbeads and the substrate. Therefore, the force F_s in Fig. 2C from interfacial tension dominates the resistance. On the basis of the experiments (movie S1) and the 3D simulation process of the interface formation (movie S2), it is found that the maximum resistance approximates to $4a\sigma_{12}$, namely

$$F_M \cos\beta > 4a\,\sigma_{12} \tag{3}$$

where β is the angle between F_M and the horizontal direction. Third, for the cube frame, the geometry and wettability requirements in Eq. 1 can be written as (section S2)

$$2 < \frac{a}{r} < 4\pi\eta\alpha\cos\theta_{123} + 2 \tag{4}$$

where α is the wettability coefficient, suggesting the ratio of the frame surface that is covered by fluid 1 and is equal to $k/2\pi$, and k is the corresponding central angle of the arc length of fluid 1 contacting with the cube frame edge (Fig. 2B). η is the surface roughness

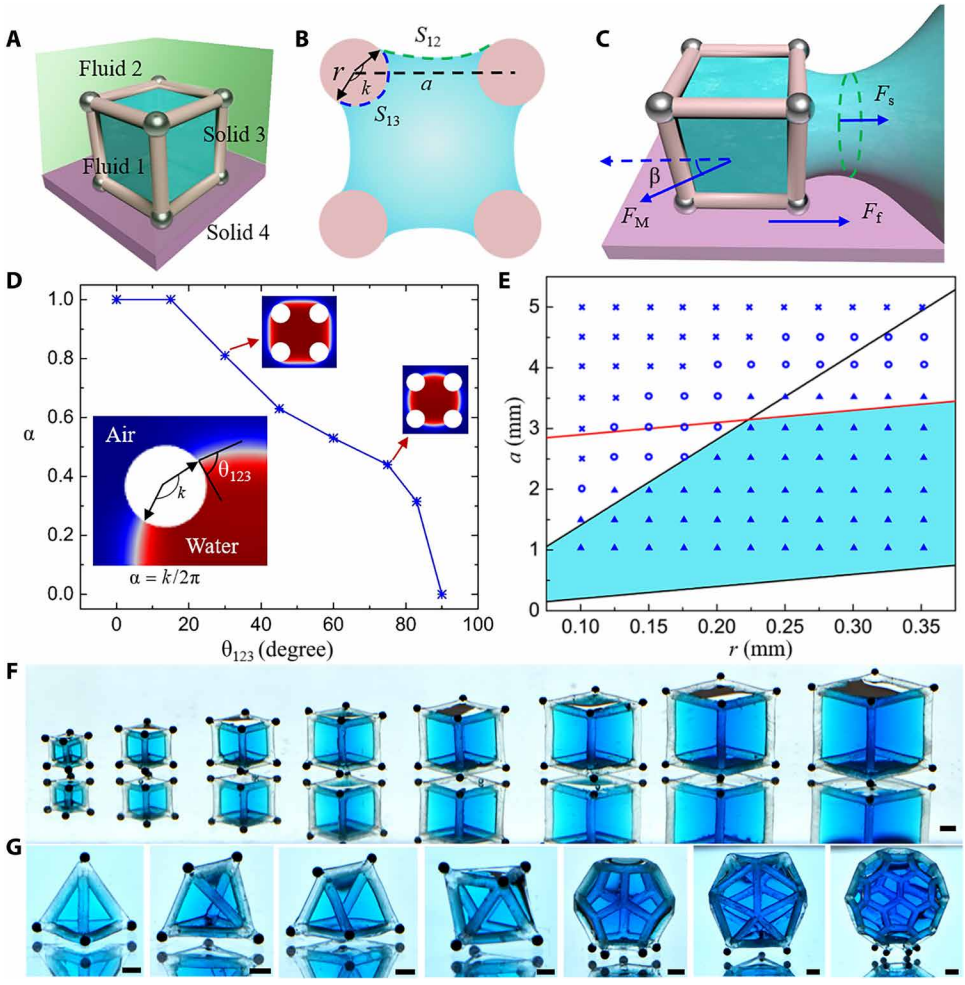

Fig. 2. Detailed design principles of the capillary container. (**A**) Fluid 1 (blue) is trapped inside of solid frame 3 (pink) and placed on solid surface 4 (purplish red) in fluid 2 (green). (**B**) Sectional view of solid frame 3 (pink) and fluid 1 (blue). (**C**) Transient state of container moving from fluid 1 to fluid 2. (**D**) Dependence of wettability coefficient α on the contact angle θ_{123} for water in air. (**E**) Effect of geometry parameters of the containers on 3D fluid interface creation for water in air. r is the frame rod radius. a is the frame side length. The red line stands for the equation of $a - 2r = 2.7$ mm. The upper and lower black lines are $a/r = 14.3$ and $a/r = 2$, respectively. The triangle, circle, and cross icons indicate stable, metastable, and failed 3D fluid interface creation, respectively. The blue region includes the safe geometry parameters for stable fluid interface creation. (**F**) Demonstration of 3D interfaces of water in silicone oil created by cube containers of different sizes. (**G**) Display of 3D interfaces of water in silicone oil created by containers with different geometries. Water was colored with blue edible dye for distinction. Scale bars, 1 mm. Photo credits: Yiyuan Zhang, University of Western Ontario.

coefficient caused by 3D printing and is slightly larger than 1. The lower bound of Eq. 4 ensures the internal space of the frame used to create the 3D fluid interface, and the upper bound of Eq. 4 is derived from the interfacial energy relationship ($E_3 < E_2$) that needs to be satisfied when using the cube frame to create a new 3D fluid interface. Last, to eliminate the capillary effect between fluid 1 and the substrate solid 4 (Fig. 2A), the wettability of the frame and solid 4 should be opposite, namely

$$\theta_{124} > 90° \quad (5)$$

where θ_{124} is the contact angle of fluid 1 on solid 4 in fluid 2.

In summary, to create the 3D fluid interface and manipulate it on a substrate with the container, Eqs. 2 to 5 should be satisfied. Equation 3 is easy to achieve by increasing the number of steel microbeads and magnetic field intensity. Meanwhile, we can readily meet Eq. 5 through wettability modifications. Equations 2 and 4 are closely related to the wettability and geometry of the frame. Taking the cube container used for "water in air" as an example, we demonstrate how to meet Eqs. 2 and 4. The parameter α in Eq. 4 is mainly determined by the container's wettability. To calculate its value, finite element modeling (FEM) is applied to quantify the dependence of α on the contact angle θ_{123} for water in air (fig. S4 and movie S3). The calculated results are summarized in Fig. 2D, indicating that α decreases from 1 to 0 as θ_{123} increases from 0 to 90°. α also determines the fluid volume that the container can capture, and the bigger α corresponds to the larger volume of the captured fluid. Given that $\eta = 1.05$, $\theta_{123} = 18°$, and the corresponding α is 0.98, the specific equations (Eqs. 2 and 4) of the cube container used for water in air are $a - 2r < 2.7$ mm and $2.0 < a/r < 14.3$ (section S2). These boundary conditions are plotted in Fig. 2E; the blue area includes the safe geometric parameters for creating the stable 3D fluid interface. To verify this conclusion, cube containers with different r and a are used. The experimental results are marked in Fig. 2E using distinct icons. The triangle represents stable 3D interface creation, the circle means metastable interface creation, and the cross indicates failed interface creation (detailed in fig. S5). It suggests that the experimental results agree with the theoretical analysis. After proper wettability modification, the cube containers are also used to create 3D interfaces of EG in air, air in water, silicone oil in water, and water in silicone oil. The experimental results are summarized in fig. S6, and their blue regions share similar trends with Fig. 2E, which proves that Eqs. 2 and 4 are applicable for many immiscible fluid pairs. On the basis of these findings, 3D interfaces of water in silicone oil (Fig. 2, F and G) and water in air (fig. S7) with diverse sizes and geometries are created to prove the container's feasibility with various structures, and their flexible dynamic manipulation is realized using a magnetic field (movie S4).

Multiple motion modes and dynamic manipulations

From a practical viewpoint, the magnetic-actuated capillary container can be seen as a multifunctional microrobot system. The container has the potential to trap specific cells, drugs, or microtissues for cell transplantation (*39*, *40*), tumor-targeting therapy (*41*), and tissue engineering (*42*). Flexible manipulation of the container is a critical step toward these goals. Hence, we studied how to steer the container to fulfill various motion behaviors. Multiple motion modes are realized by tuning the distribution of steel microbeads and the magnetic field motion. The cube container that captured water in silicone oil is used to elaborate the influence of steel microbead distribution on the movement modes (Fig. 3). The container performs a complex rotation and flipping motion (Fig. 3A and movie S5) when only one steel bead is attached to the cube vertex. Under the control of the magnetic field, the steel microbead is magnetized and drives the container to rotate and flip on three sides around the microbead (section S3). A simpler flipping motion is exhibited by attaching two steel microbeads to adjacent vertices of the frame (Fig. 3B and movie S6). In this case, the container always flips back and forth regularly around the edge that is attached with steel microbeads. In addition, the container can perform a single-axis rotation around a cube edge when two steel microbeads are attached to the cube diagonal vertices (Fig. 3C and movie S7). These motion modes are useful to change the angle of view for the trapped object observation. As the number of steel microbeads increases, the degrees of freedom of the cube container decrease, and its motion tends to be more stable and simpler. Thus, the container with four steel microbeads attached to vertices of one cube face behaves in a stable translation (Fig. 3D and movie S8). Their underlying mechanical mechanisms are discussed in section S3.

The capillary container not only can be manipulated on the horizontal surface but also can transport on the upright surface. The antigravity transportation of a cube container loaded with water in air is displayed in Fig. 3E and movie S9. Moreover, droplet release is vital for many biomedical applications including biochemical sensing, detection, and high-throughput screening (*43*). Here, we demonstrate the droplet release (Fig. 3F) by designing the wettability difference between the container (θ_{123}) and solid surface (θ_{124}). θ_{123} is 50°, and θ_{124} is 10°. Therefore, the water can be released on the substrate because of the wettability gradient (*44*). The water sampling and releasing process is illustrated in movie S10. These multiple motion modes and manipulations of the container would be promising for many biotechnologies including cell delivery (*39*, *40*), microbiology observation and sorting (*10*), and precise targeting therapy (*41*).

Versatility in different fluids for microfluidics and chemical applications

To demonstrate the feasibility of the capillary container in various fluidic environments, we applied them in four kinds of immiscible fluid systems to operate selective fluid collections and chemical reactions. With proper hydrophobization, the container can capture gas bubbles in water (Fig. 4A and movie S11). Similarly, the hydrophilic container is able to collect water droplets placed in silicone oil (Fig. 4B and movie S12). These fluid interface manipulations open potential practical applications in removing unnecessary bubbles in microfluidic channels and selectively collecting target fluids in open-space microfluidics. In addition, precise sampling, lossless liquid reagents transport (*45*), and flexible droplet manipulation (*46*) in different conditions are critical for analytical chemistry, biotechnology, and disease diagnostic. Here, we performed three kinds of chemical reactions with the container. Figure 4C depicts a catalytic reaction in silicone oil, namely, the catalytic decomposition of H_2O_2. The aqueous solutions of H_2O_2 and ferric chloride were first placed in the oil. A hydrophilic container was used to capture H_2O_2 and transport it into the $FeCl_3$ aqueous solution to perform the catalytic reaction, which produced many oxygen bubbles and brown-red iron hydroxide (movie S13). Likewise, the container can manipulate oils in water. Figure 4D exemplifies an organic reaction in water. First, bromine and styrene were dissolved in CCl_4 and placed in water.

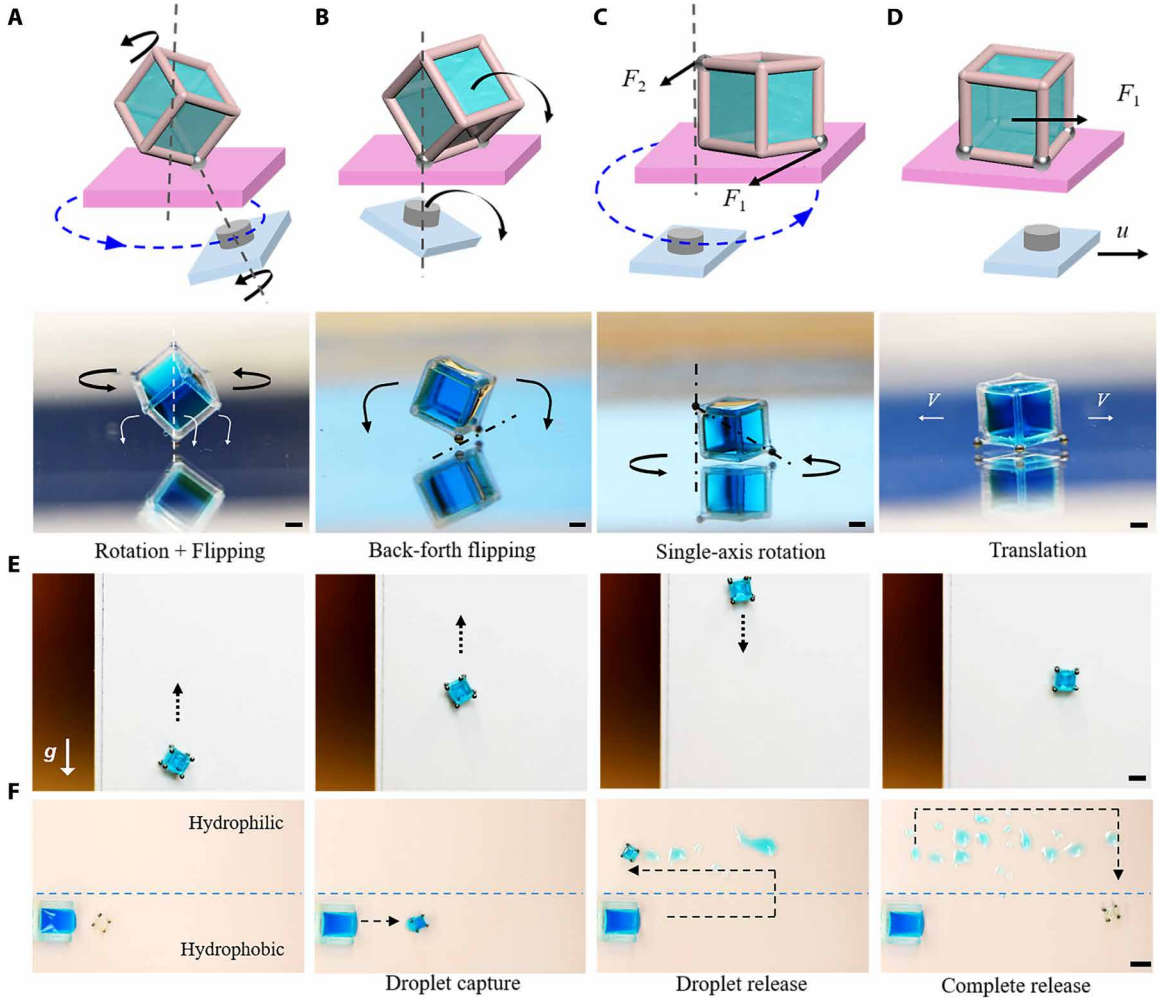

Fig. 3. Dynamic manipulations of the capillary container. (**A** to **D**) Diverse moving modes of containers loaded with water in silicone oil with differentiated steel microbead distribution. Scale bars, 1 mm. (A) Rotation and flipping around the microbead with only one steel microbead attached to the cube vertex. (B) Flipping back and forth around one edge with two steel microbeads attached to vertices located at one cube edge. (C) Single-axis rotation with two steel microbeads attached to vertices located at the cube diagonal. F_1 and F_2 represent the magnetic forces of the lower and upper steel microbeads in the magnetic field, respectively. (D) Translation movement with four steel microbeads attached to vertices located at one cube face. F_1 is the magnetic driving force; u is the translation velocity. (**E**) Antigravity transportation of a water droplet on the upright hydrophobic surface. Scale bar, 2 mm. (**F**) Water droplet release on a surface in the air. The container captures a water droplet on the hydrophobic part of the surface and then releases it on the hydrophilic zone of the surface. Scale bar, 4 mm. Water was colored with blue edible dye for distinction. Photo credits: Yiyuan Zhang, University of Western Ontario.

A hydrophobic container was used to sample the orange Br_2/CCl_4 and deliver it into styrene/CCl_4. The color soon faded because of the addition reaction (movie S14). During these reactions, the container can rotate as a mixer to speed up the reaction. Besides, because the containers can trap and store a certain amount of fluid, they are useful for multistep reactions research, by carrying the product in one step to the next step as a reactant (Fig. 4E and movie S15). First, water was captured by a hydrophilic container and transported to dissolve the $CaCl_2$ powder. Next, the $CaCl_2$ solution was transported into the Na_2CO_3 solution and generated the calcium carbonate precipitation. Last, part of the $CaCO_3$ precipitation was carried into dilute hydrochloric acid for dissolution and generating CO_2 bubbles. Such a remote manipulation mechanism will facilitate much chemical reaction research that involves hazardous or toxic reactants or products, and the under-liquid reaction manipulation will benefit applications where air-sensitive reagents (*47*) are applied.

Liquid packaging and membrane preparation for drug release study

As mentioned above, the capillary container can capture and store liquid with a predesigned shape. Actually, it is more important to preserve or freeze-in the shaped liquid interface for protecting and isolating the material of interest (*48*–*50*). In the last part, we used the container to achieve liquid packaging via the interfacial reaction and explore its potential in drug delivery and release applications. The basic liquid packaging process using the container is displayed in Fig. 5A. First, a droplet of solution *A* is trapped by the container and then immersed in solution *B*. The chemical reaction between solution *A* and solution *B* such as interfacial polymerization or gelation will solidify the fluid interface and form the membrane structure. Thus, solution *A* can be encapsulated in the container developing a stable "liquid core–membrane shell" structure. Here, the liquid package is completed via the reticulation process between sodium

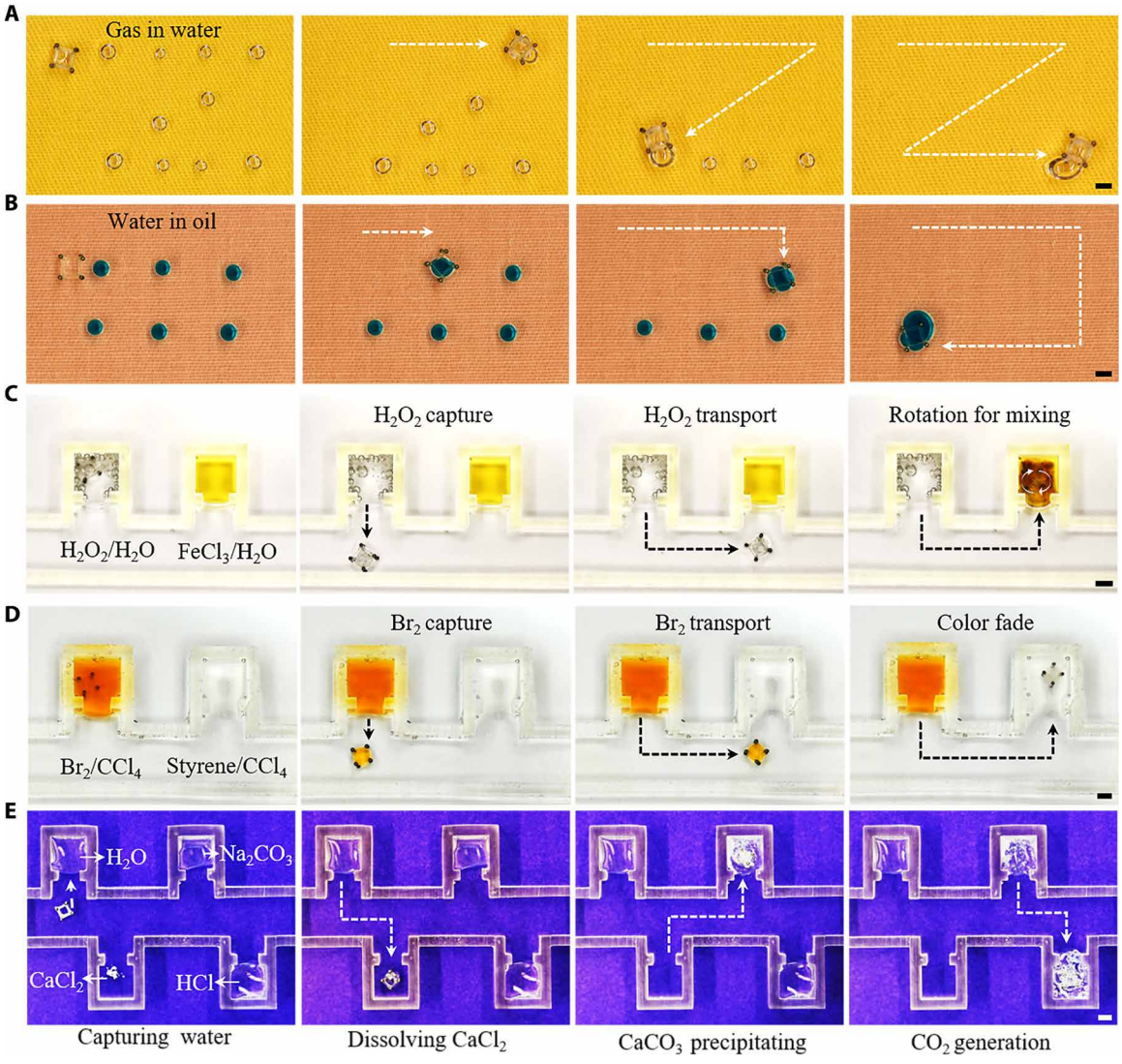

Fig. 4. Versatility in different fluids for microfluidics and chemical applications. (**A**) Gas collection in water. A hydrophobic container is used to capture gas bubbles (1 to 2 μl) distributed in a zigzag pattern in the water on hydrophobic glass. (**B**) Water collection in silicone oil. The hydrophilic container is used to collect blue edible dye–colored water droplets (4 μl) placed in silicone oil on hydrophobic glass. (**C**) Catalytic reaction in oil. Liquids in the U-shaped grooves are water-dissolved with H_2O_2 (left, 200 μl) and $FeCl_3$ (right, 200 μl), respectively. A droplet of H_2O_2/H_2O is captured by the container and transported to $FeCl_3/H_2O$. (**D**) Organic reaction in water. Liquids in the U-shaped grooves are CCl_4-dissolved with Br_2 (left, 200 μl) and styrene (right, 200 μl), respectively. The container traps a droplet of Br_2/CCl_4 and transports it to styrene/CCl_4. (**E**) Multistep reactions. The container captures a water droplet and uses it to dissolve the $CaCl_2$ powder; then, the $CaCl_2$-dissolved droplet is transported in $NaCO_3$. After a short reaction time, the container traps part of the generated $CaCO_3$ precipitation and transports it in the dilute hydrochloric acid. Scale bars, 2 mm. Photo credits: Yiyuan Zhang, University of Western Ontario.

alginate and $CaCl_2$. Moreover, a free-standing 3D membrane structure is obtained after the core liquid drying as shown in Fig. 5B. With the critical point drying method, the membrane structures can be preserved. As the scanning electron microscopy (SEM) images (Fig. 5, C and D) show, the membrane exhibits a porous network structure, with a pore size of about 50 nm. A variety of free-standing 3D membrane structures (Fig. 5E) were prepared using containers with diverse geometries. These dry membranes can be rehydrated after soaking in water, and the semipermeable membrane will permit ions and water molecules to reenter the container. For practical applications, the encapsulation function of the capillary container can be used to package bioactive proteins, enzymes, or microorganisms for the research of protein functional control (*51*), biocatalysis (*52*), or probiotic bacteria (*53*), and these bioactive objects can be freeze-dried and preserved in the container for storage and transportation. Meanwhile, it is convenient to reactivate them when needed.

To visualize the substance release across the membrane, we colored the $CaCl_2$ solution with red edible dye. The slow dye release process is illustrated in Fig. 5F. The color gradually fades with time and becomes colorless after 4 hours. The dye release processes without and with liquid packaging are compared. The former displays a quick diffusion and mixing process, while the latter shows a slow-release process (movie S16). Next, we take riboflavin (vitamin B_2) as an example to demonstrate the drug release application. Riboflavin is

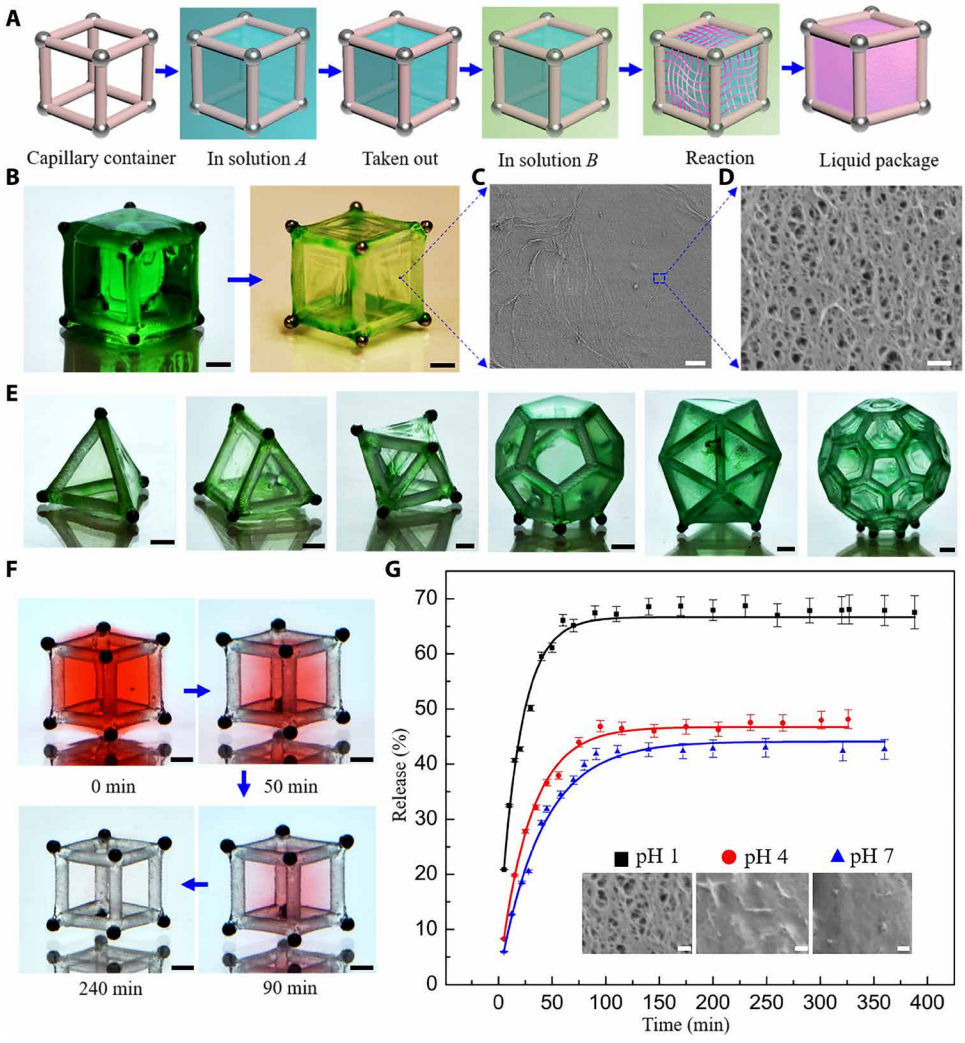

Fig. 5. Drug release application with the capillary container. (**A**) Schematic diagram of the liquid packaging process. A droplet of solution *A* is first captured by the container and then immersed in solution *B*. The interfacial reactions between solution *A* and *B* will solidify the fluid interface and form a membrane; then, solution *A* is packaged in the container. (**B**) A free-standing 3D membrane structure was obtained after the core liquid drying. Scale bars, 1 mm. (**C** and **D**) SEM images of the membrane after critical point drying. Scale bars, 4 μm (C) and 200 nm (D). (**E**) Diverse free-standing 3D membrane structures obtained using containers with different geometries after core liquid drying. (**F**) Slow red edible dye release process in water after package by the cube container. Scale bars, 1 mm. (**G**) Release profiles and theoretical fitting curves of riboflavin packaged in the icosahedron containers in distilled water with different pH. The insets in the figure show the SEM images of the membranes treated with critical point drying after drug release in distilled water with different pH. Scale bars, 100 nm. Photo credits: Yiyuan Zhang, University of Western Ontario.

an indispensable vitamin for maintaining the body's energy supply and is vital in treating diseases including migraines, corneal disorders, and homocysteinemia. Riboflavin is first dissolved in the $CaCl_2$ solution and then packaged in the icosahedron containers using interfacial gelation. The dynamic release of the packaged riboflavin was studied in distilled water with different pH at room temperature. The release profiles are illustrated in Fig. 5G. It suggests that the release rate and equilibrium concentration increases with the decrease of pH. The growing release rate is induced by the reduced membrane thickness and increased porosity and pore size because the hydrogel membranes shrink and are partially hydrolyzed by proton exchange in acidic solution (*54*–*56*). To verify these changes, we compared the transmittance of the wet membranes under natural light (fig. S8). It shows that their transmittances increased with pH decreasing, reflecting their diminished thickness. Besides, after the drug release, the 3D hydrogel membranes were treated with critical point drying for SEM imaging. It is proved that there is a remarkable increase in porosity and pore size of the hydrogel membranes with decreasing pH (insets in Fig. 5G and fig. S9). Theoretically, the icosahedron containers can be simplified and approximated to a homogeneous sphere, so the release kinetics can be analyzed by fitting the experimental data with a sphere diffusion model as follows (*57*)

$$C_t = C_{eq}(1 - k_1 \exp(-k_2(t - t_0))) \quad (6)$$

where C_t is the riboflavin concentration in the bulk solution after time t, C_{eq} is the equilibrium concentration of riboflavin in the bulk solution, k_1 is a constant related to the ratio of the volumes of solution and sphere, and k_2 is a constant related to the diffusion constant D_m.

By fitting the experimental data with the theoretical model, the value of C_{eq} and D_m is determined (table S2), and both C_{eq} and D_m increase with the decreasing pH, agreeing well with the experiments. Our results suggest that the capillary container is anticipated to be a versatile platform to perform efficient liquid packaging, delivery, storage, and 3D membrane production, which offers promising routes for encapsulation, lab-in-a-drop, delivery vehicles, and biochemical reactors.

DISCUSSION

In conclusion, we have developed a multifunctional magnetic-actuated capillary container to achieve structured 3D fluid interface creation and flexible manipulation for various applications. The wettability and geometry of the container dominate the type, size, and shape of the created fluid interface; steel microbead distribution and magnetic field motion govern its moving behaviors including flipping, rotation, and translation. With proper wettability difference design, the liquid release is also realized. Moreover, we elaborated the universality and effectiveness of the container with a sequence of experiments including selective fluid collection and chemical reaction manipulations in different immiscible fluid systems. The container is also effective in miscible fluids, making it feasible to do liquid packaging via interfacial gelation for drug release study. We envisage that this multifunctional magnetic-actuated capillary container could help unravel the mechanisms of numerous fundamental fluid interfacial processes and contribute to applications involving fluid sampling, transport, mixing, release, storage, and packaging.

Compared with conventional microfluidics, the capillary container has some distinctive advantages in fluid handling and biological applications. (i) The capillary container is easy to manufacture and use, eliminating bubble trapping and clogging problems. (ii) It is suitable for studying large biological samples, such as multicellular spheroids and tissue sections, without destroying their spatial structures. (iii) Once the target samples are captured by the capillary container, they can be regarded as an independent research unit and can be operated independently. The unit can be flexibly transported, rotated, flipped, released, stored, and packaged according to specific needs. (iv) Biological samples in the capillary container can directly contact the fluid of interest and can be selectively stimulated with biophysics or biochemistry factors. Samples of interest can be selectively extracted for analysis. (v) The capillary container can create a stable 3D fluid interface, thereby providing a platform for the research of biological fluid interface problems, such as respiratory toxicology research. Besides, compared with usual open microfluidic strategies, the capillary container is user-friendly and extensible, does not require complex and expensive equipment, and can be easily customized for different needs.

Our findings also provide ample inspiration for expanding the container's applications into other fields. Starting from the change of structure and composition of the container, many works can be done in the future. If we printed the frame with biocompatible materials, the container could be used in vivo. Combined with high-resolution printing and magnetic coating, microscale magnetic-actuated capillary containers can be fabricated and could find applications in microfluidics or blood vessels to do targeting operations. It is also possible to produce intricate frame structures to imitate natural complex 3D fluid interfaces, which would pose opportunities to address long-standing conundrums such as lung function (*58*), cell signaling (*59*), and cell division (*60*). Furthermore, plentiful biomedical applications will emerge from the integration of the membrane and the container by interfacial reactions. The packaged container creates a stable inner environment that isolates the materials of interest from the external environment but will not block their interaction with a permeable membrane. This structure would open promising avenues for bioactive material encapsulation including enzymes, vaccines, antigens, hormones, proteins, cells, tissues, and even mini organs to fulfill various needs in biomedicine (*42*, *51*, *52*). Besides, functionalization of membrane, frames, or liquid contents of the container with stimuli-responsive materials such as quantum dots or smart polymers would open new routes for next-generation clinical therapy using microrobots.

MATERIALS AND METHODS

Preparation of the magnetic-actuated capillary container

The magnetic-actuated capillary container consists of a 3D printed solid frame and steel microbeads. All solid frames are printed with an Asiga Freeform Pico 2 printer using the commercial resin PlasCLEAR V2. The steel microbeads have a diameter of 500 μm and were attached to the vertices of printed polyhedral frames with the superglue. The container is manipulated by a homemade magnetic control system. Magnets were placed on a motorized precise translation stage, which is a part of a commercial laser engraving machine. The stage can drive the magnet to move in a prescribed path defined in the path planning software of the machine. The moving direction and speed can be precisely adjusted. Multiple motion modes such as translation, reciprocating movement, and rotation can be easily achieved.

Surface modifications

Two different surface modifications were applied to the capillary containers for the manipulation of various fluids. To obtain the hydrophilic wettability, containers were treated with the ultraviolet (UV)/ozone cleaner at 60°C for 2 hours. After the hydrophilic treatment, the hydrophobic containers were obtained by modifying the hydrophilic containers with 1*H*,1*H*,2*H*,2*H*-perfluorodecyltrimethoxysilane using chemical vapor deposition at 90°C for 3 hours. Hydrophobic glass substrates were obtained by the same treatment. The wettability can be varied by adjusting the temperature and times.

Liquid preparation for fluid interface manipulation and chemical reactions

In Fig. 1, the water droplets captured in the containers are pure water mixed with blue edible dye in a volume ratio of 100:1. The EG droplets are EG-colored by a green edible dye with a volume ratio of 100:1. The captured silicone oil is added with Sudan III in a concentration of 0.01 M. The H_2O_2/H_2O solution used in Fig. 4C is 30% hydrogen peroxide solution, and the concentration of the $FeCl_3/H_2O$ solution is 0.1 M. The concentrations of the Br_2/CCl_4 and styrene/CCl_4 solution in Fig. 4D are 0.1 M. In Fig. 4E, the liquids used are pure water, 0.1 M Na_2CO_3, and 0.1 M HCl solutions.

Liquid packaging and membrane preparation for drug release study

The concentrations of $CaCl_2$ and sodium alginate solutions used in Fig. 5 for liquid packaging are all 1 wt %. To get the 3D membrane structure in Fig. 5 (B and E), the $CaCl_2$-loaded containers with

different geometries were dripped into the sodium alginate bath for 2 min. They are then put on a hydrophobic glass sheet and dried naturally in the air after washing twice with distilled water. To obtain a green-colored membrane, the $CaCl_2$ and sodium alginate solutions are colored by a blue and yellow edible dye with a volume ratio of 100:1, respectively. For the slow-release process displayed in Fig. 5F, the red dye–colored $CaCl_2$ droplet was first captured by the cube container, then dripped into the sodium alginate bath for 1 min, and washed with distilled water. Next, after stabilizing in the $CaCl_2$ solution for 1 min, the membrane-packaged container was put in 120 ml of water to show the slow process of dye release. The release of riboflavin shown in Fig. 5G was carried out using the Varian Cary 100 Bio UV-Vis Spectrophotometer. Riboflavin (5 mg/100 ml) was first dissolved in the $CaCl_2$ solution. The icosahedral containers were dripped into the riboflavin dissolved $CaCl_2$ solution and then taken out; every container was filled with the solution by capillary force. Next, the drug-loaded containers were dripped into the sodium alginate bath near the liquid surface under stirring for 10 min. After washing with distilled water, they were rinsed in $CaCl_2$ solution for 10 min to stabilize the hydrogel membrane. Later, three batches of the same number of the packaged containers were placed into 20 ml of distilled water with pH of 1, 4, and 7 after washing twice with distilled water. HCl (1 M) was used to prepare the water solutions with pH of 1 and 4. At scheduled time intervals, the amount of released riboflavin was determined from solution absorbance at 444-nm wavelength. After the riboflavin release profile data collection, membranes on the containers were treated with critical point drying using K850 Critical Point Dryer with CO_2. Ethanol was used as the solvent during the dehydration. The microstructures of the dried membranes were characterized by SEM.

Numerical simulation

The 3D water-air fluid interface formation (movie S2) was simulated by the pseudopotential two-phase lattice Boltzmann method. The computational domain sizes are 12 mm × 6 mm × 6 mm and 12 mm × 9 mm × 9 mm, respectively, while water is occupied from 2 to 12 mm in the x direction. Cube containers with two different sizes are immersed in water with a constant contact angle of 30°. The center of the cube container locates at 5 mm along the central line of the x axis. The side lengths of the cube container are 2.0 and 3.5 mm, respectively, while their diameter is the same as 300 μm. The left side of the computational domain is set as stationary, while the right is given a constant velocity v_0. The remaining four sides are set as periodic. Gravity is given in the x direction. Instead of moving the cube container out of the water as in the experiment, we move the water by giving the velocity v_0 at the right side of the domain. To model the slow movement of the container physically, we only let the water move 0.5 μm per iteration in the simulations. When the container is moving from water to air, water in the small container is captured, while water in the larger container is replaced by air. The smaller container makes a higher capillary force, which is strong enough to balance the gravitational force. The FEM simulations of the creation of water-in-air interface with the container (movie S3) were performed using COMSOL Multiphysics 5.4. The two-phase flow and phase-field module were used. The moving mesh was set at a velocity of 1 mm/s. The contact angle of water on the solid frame (θ_{123}) varies from 0° to 90°, and the corresponding α is calculated, as shown in fig. S4 and Fig. 2D. The 2D model was used for simplifications. It suggests that α decreases with the increase of θ_{123}, and the captured fluid volume also reduces.

SUPPLEMENTARY MATERIALS

Supplementary material for this article is available at http://advances.sciencemag.org/cgi/content/full/7/34/eabi7498/DC1

REFERENCES AND NOTES

1. J. Worden, D. Noone, K. Bowman, Importance of rain evaporation and continental convection in the tropical water cycle. *Nature* **445**, 528–532 (2007).
2. P. Tao, G. Ni, C. Song, W. Shang, J. Wu, J. Zhu, G. Chen, T. Deng, Solar-driven interfacial evaporation. *Nat. Energy* **3**, 1031–1041 (2018).
3. A.-H. Cavusoglu, X. Chen, P. Gentine, O. Sahin, Potential for natural evaporation as a reliable renewable energy resource. *Nat. Commun.* **8**, 617 (2017).
4. H. Sirringhaus, T. Kawase, R. H. Friend, T. Shimoda, M. Inbasekaran, W. Wu, E. P. Woo, High-resolution inkjet printing of all-polymer transistor circuits. *Science* **290**, 2123–2126 (2000).
5. J.-U. Park, M. Hardy, S. J. Kang, K. Barton, K. Adair, D. k. Mukhopadhyay, C. Y. Lee, M. S. Strano, A. G. Alleyne, J. G. Georgiadis, P. M. Ferreira, J. A. Rogers, High-resolution electrohydrodynamic jet printing. *Nat. Mater.* **6**, 782–789 (2007).
6. D. Guo, Y. Li, X. Zheng, F. Li, S. Chen, M. Li, Q. Yang, H. Li, Y. Song, Programmed coassembly of one-dimensional binary superstructures by liquid soft confinement. *J. Am. Chem. Soc.* **140**, 18–21 (2018).
7. F. Frausher, A. klauser, E. J. Halpern, W. Horninger, G. Bartsch, Detection of prostate cancer with a microbubble ultrasound contrast agent. *Lancet* **357**, 1849–1850 (2001).
8. K. W. Ferrara, M. A. Borden, H. Zhang, Lipid-shelled vehicles: Engineering for ultrasound molecular imaging and drug delivery. *Acc. Chem. Res.* **42**, 881–892 (2009).
9. A. Ozcelik, J. Rufo, F. Guo, Y. Gu, P. Li, J. Lata, T. J. Huang, Acoustic tweezers for the life sciences. *Nat. Methods* **15**, 1021–1028 (2018).
10. D. Ahmed, A. Ozcelik, N. Bojanala, N. Nama, A. Upadhyay, Y. Chen, W. Hanna-Rose, T. J. Huang, Rotational manipulation of single cells and organisms using acoustic waves. *Nat. Commun.* **7**, 11085 (2016).
11. Z. Cai, S. Zhao, Z. Huang, Z. Li, M. Su, Z. Zhang, Z. Zhao, X. Hu, Y.-S. Wang, Y. Song, Bubble architectures for locally resonant acoustic metamaterials. *Adv. Funct. Mater.* **29**, 1906984 (2019).
12. Z. Huang, S. Zhao, M. Su, Q. Yang, Z. Li, Z. Cai, H. Zhao, X. Hu, H. Zhou, F. Li, J. Yang, Y. Wang, Y. Song, Bioinspired patterned bubbles for broad and low-frequency acoustic blocking. *ACS Appl. Mater. Interfaces* **12**, 1757–1764 (2020).
13. F. Zhang, J.-b. Fan, S. Wang, Interfacial polymerization: From chemistry to functional materials. *Angew. Chem. Int. Ed.* **59**, 21840–21856 (2020).
14. K. Piradashvili, E. M. Alexandrino, F. R. Wurm, K. Landfester, Reactions and polymerizations at the liquid–liquid interface. *Chem. Rev.* **116**, 2141–2169 (2016).
15. J. Siepmann, F. Siepmann, Modeling of diffusion controlled drug delivery. *J. Control. Release* **161**, 351–362 (2012).
16. Z. Liang, W. Bu, K. J. Schweighofer, D. J. Walwark, J. S. Harvey, G. R. Hanlon, D. Amoanu, C. Erol, I. Benjamin, M. L. Schlossman, Nanoscale view of assisted ion transport across the liquid–liquid interface. *Proc. Natl. Acad. Sci. U.S.A.* **116**, 18227–18232 (2019).
17. X. Hou, Y. Hu, A. Grinthal, M. Khan, J. Aizenberg, Liquid-based gating mechanism with tunable multiphase selectivity and antifouling behaviour. *Nature* **519**, 70–73 (2015).
18. Z. Sheng, J. Zhang, J. Liu, Y. Zhang, X. Chen, X. Hou, Liquid-based porous membranes. *Chem. Soc. Rev.* **49**, 7907–7928 (2020).
19. I. Ali, V. Gupta, Advances in water treatment by adsorption technology. *Nat. Protoc.* **1**, 2661–2667 (2006).
20. B. J. Shean, J. J. Cilliers, A review of froth flotation control. *Int. J. Miner. Process.* **100**, 57–71 (2011).
21. E. Dickinson, Food emulsions and foams: Stabilization by particles. *Curr. Opin. Colloid Interface Sci.* **15**, 40–49 (2010).
22. T. T. Al-Housseiny, P. A. Tsai, H. A. Stone, Control of interfacial instabilities using flow geometry. *Nat. Phys.* **8**, 747–750 (2012).
23. I. Bischofberger, R. Ramachandran, S. R. Nagel, Fingering versus stability in the limit of zero interfacial tension. *Nat. Commun.* **5**, 5265 (2014).
24. J. Forth, P. Y. Kim, G. Xie, X. Liu, B. A. Helms, T. P. Russell, Building reconfigurable devices using complex liquid–fluid interfaces. *Adv. Mater.* **31**, 1806370 (2019).
25. S. Shi, T. P. Russell, Nanoparticle assembly at liquid–liquid interfaces: From the nanoscale to mesoscale. *Adv. Mater.* **30**, 1800714 (2018).
26. T. M. Squires, S. R. Quake, Microfluidics: Fluid physics at the nanoliter scale. *Rev. Mod. Phys.* **77**, 977–1026 (2005).
27. J. Atencia, D. J. Beebe, Controlled microfluidic interfaces. *Nature* **437**, 648–655 (2005).
28. Z. Huang, M. Su, Q. Yang, Z. Li, S. Chen, Y. Li, X. Zhou, F. Li, Y. Song, A general patterning approach by manipulating the evolution of two-dimensional liquid foams. *Nat. Commun.* **8**, 14110 (2017).

29. Z. Huang, Q. Yang, M. Su, Z. Li, X. Hu, Y. Li, Q. Pan, W. Ren, F. Li, Y. Song, A general approach for fluid patterning and application in fabricating microdevices. *Adv. Mater.* **30**, 1802172 (2018).
30. J. Li, N. S. Ha, T. L. Liu, R. M. van Dam, C.-J. '. C.'. Kim, Ionic-surfactant-mediated electro-dewetting for digital microfluidics. *Nature* **572**, 507–510 (2019).
31. H. Dai, C. Gao, J. Sun, C. Li, N. Li, L. Wu, Z. Dong, L. Jiang, Controllable high-speed electrostatic manipulation of water droplets on a superhydrophobic surface. *Adv. Mater.* **31**, 1905449 (2019).
32. S. P. Zhang, J. Lata, C. Chen, J. Mai, F. Guo, Z. Tian, L. Ren, Z. Mao, P.-H. Huang, P. Li, S. Yang, T. J. Huang, Digital acoustofluidics enables contactless and programmable liquid handling. *Nat. Commun.* **9**, 2928 (2018).
33. P. Zhang, C. Chen, X. Su, J. Mai, Y. Gu, Z. Tian, H. Zhu, Z. Zhong, H. Fu, S. Yang, K. Chakrabarty, T. J. Huang, Acoustic streaming vortices enable contactless, digital control of droplets. *Sci. Adv.* **6**, eaba0606 (2020).
34. W. Wang, J. V. I. Timonen, A. Carlson, D.-M. Drotlef, C. T. Zhang, S. Kolle, A. Grinthal, T.-S. Wong, B. Hatton, S. H. Kang, S. Kennedy, J. Chi, R. T. Blough, M. Sitti, L. Mahadevan, J. Aizenberg, Multifunctional ferrofluid-infused surfaces with reconfigurable multiscale topography. *Nature* **559**, 77–82 (2018).
35. S. Ben, T. Zhou, H. Ma, J. Yao, Y. Ning, D. Tian, K. Liu, L. Jiang, Multifunctional magnetocontrollable superwettable-microcilia surface for directional droplet manipulation. *Adv. Sci.* **6**, 1900834 (2019).
36. A. Li, H. Li, Z. Li, Z. Zhao, K. Li, M. Li, Y. Song, Programmable droplet manipulation by a magnetic-actuated robot. *Sci. Adv.* **6**, eaay5808 (2020).
37. P.-G. De Gennes, F. Brochard-Wyart, D. Quéré, *Capillarity and Wetting Phenomena: Drops, Bubbles, Pearls, Waves* (Springer Science & Business Media, 2013).
38. D. G. A. L. Aarts, Capillary length in a fluid–fluid demixed colloid–polymer mixture. *J. Phys. Chem. B* **109**, 7407–7411 (2005).
39. S. Jeon, S. Kim, S. Ha, S. Lee, E. Kim, S. Y. Kim, S. H. Park, J. H. Jeon, S. W. Kim, C. Moon, B. J. Nelson, J.-y. Kim, S.-W. Yu, H. Choi, Magnetically actuated microrobots as a platform for stem cell transplantation. *Sci. Robot.* **4**, eaav4317 (2019).
40. J. Li, X. Li, T. Luo, R. Wang, C. Liu, S. Chen, D. Li, J. Yue, S.-h. Cheng, D. Sun, Development of a magnetic microrobot for carrying and delivering targeted cells. *Sci. Robot.* **3**, (eaat8829, 2018).
41. D. Li, H. Choi, S. Cho, S. Jeong, Z. Jin, C. Lee, S. Y. Ko, J.-O. Park, S. Park, A hybrid actuated microrobot using an electromagnetic field and flagellated bacteria for tumor-targeting therapy. *Biotechnol. Bioeng.* **112**, 1623–1631 (2015).
42. T. Desai, L. D. Shea, Advances in islet encapsulation technologies. *Nat. Rev. Drug Discov.* **16**, 338–350 (2017).
43. W. Wang, C. Yang, Y. Liu, C. M. Li, On-demand droplet release for droplet-based microfluidic system. *Lab Chip* **10**, 559–562 (2010).
44. Y.-H. Lai, M.-H. Hsu, J.-T. Yang, Enhanced mixing of droplets during coalescence on a surface with a wettability gradient. *Lab Chip* **10**, 3149–3156 (2010).
45. S. Huang, J. Li, L. Liu, L. Zhou, X. Tian, Lossless fast drop self-transport on anisotropic omniphobic surfaces: Origin and elimination of microscopic liquid residue. *Adv. Mater.* **31**, 1901417 (2019).
46. Y. Zuo, L. Zheng, C. Zhao, H. Liu, Micro-/nanostructured interface for liquid manipulation and its applications. *Small* **16**, 1903849 (2020).
47. D. F. Shriver, M. A. Drezdzon, *The Manipulation of Air-Sensitive Compounds* (John Wiley & Sons, 1986).
48. S. Coppola, G. Nasti, V. Vespini, L. Mecozzi, R. Castaldo, G. Gentile, M. Ventre, P. A. Netti, P. Ferraro, Quick liquid packaging: Encasing water silhouettes by three-dimensional polymer membranes. *Sci. Adv.* **5**, eaat5189 (2019).
49. M. Cui, T. Emrick, T. P. Russell, Stabilizing liquid drops in nonequilibrium shapes by the interfacial jamming of nanoparticles. *Science* **342**, 460–463 (2013).
50. D. Kumar, J. D. Paulsen, T. P. Russell, N. Menon, Wrapping with a splash: High-speed encapsulation with ultrathin sheets. *Science* **359**, 775–778 (2018).
51. D. Fujita, K. Suzuki, S. Sato, M. Yagi-Utsumi, Y. Yamaguchi, N. Mizuno, T. Kumasaka, M. Takata, M. Noda, S. Uchiyama, K. Kato, M. Fujita, Protein encapsulation within synthetic molecular hosts. *Nat. Commun.* **3**, 1093 (2012).
52. L. Betancor, H. R. Luckarift, Bioinspired enzyme encapsulation for biocatalysis. *Trends Biotechnol.* **26**, 566–572 (2008).
53. K. Sultana, G. Godward, N. Reynolds, R. Arumugaswamy, P. Peiris, K. Kailasapathy, Encapsulation of probiotic bacteria with alginate–starch and evaluation of survival in simulated gastrointestinal conditions and in yoghurt. *Int. J. Food Microbiol.* **62**, 47–55 (2000).
54. S. T. Moe, G. Skjaak-Braek, A. Elgsaeter, O. Smidsroed, Swelling of covalently crosslinked alginate gels: Influence of ionic solutes and nonpolar solvents. *Macromolecules* **26**, 3589–3597 (1993).
55. K. I. Draget, G. Skjåk-Bræk, B. E. Christensen, O. Gåserød, O. Smidsrød, Swelling and partial solubilization of alginic acid gel beads in acidic buffer. *Carbohydr. Polym.* **29**, 209–215 (1996).
56. G. Ben Messaoud, L. Sánchez-González, L. Probst, C. Jeandel, E. Arab-Tehrany, S. Desobry, Physico-chemical properties of alginate/shellac aqueous-core capsules: Influence of membrane architecture on riboflavin release. *Carbohydr. Polym.* **144**, 428–437 (2016).
57. J. Crank, *The Mathematics of Diffusion* (Oxford Univ. Press, 1979).
58. B. Grigoryan, S. J. Paulsen, D. C. Corbett, D. W. Sazer, C. L. Fortin, A. J. Zaita, P. T. Greenfield, N. J. Calafat, J. P. Gounley, A. H. Ta, F. Johansson, A. Randles, J. E. Rosenkrantz, J. D. Louis-Rosenberg, P. A. Galie, K. R. Stevens, J. S. Miller, Multivascular networks and functional intravascular topologies within biocompatible hydrogels. *Science* **364**, 458–464 (2019).
59. P. Li, S. Banjade, H.-C. Cheng, S. Kim, B. Chen, L. Guo, M. Llaguno, J. V. Hollingsworth, D. S. King, S. F. Banani, P. S. Russo, Q.-X. Jiang, B. T. Nixon, M. K. Rosen, Phase transitions in the assembly of multivalent signalling proteins. *Nature* **483**, 336–340 (2012).
60. J. M. Scholey, I. Brust-Mascher, A. Mogilner, Cell division. *Nature* **422**, 746–752 (2003).

Acknowledgments

Funding: J.Y. is grateful for the financial support from Ontario Research Fund–Research Excellence (ORF-RE #09-078) and Natural Sciences and Engineering Research Council of Canada (NSERC: RGPIN-2016-05198). Y.Z. is grateful for the financial support from the China Scholarship Council (CSC) from the Ministry of Education of P.R. China. **Author contributions:** Y.Z., Z.H., and J.Y. conceived and designed the experiments. Y.Z. and Z.H. did the fluid interface creation and manipulation experiments. Z.H., F.Q., and Z.C. conducted the numerical simulations of the fluid interface formation. Y.Z., Y.Y., Z.L., and J.X. performed the characterization experiments. Y.Z., Z.H., J.Y., D.Z., Q.G., and Y.S. wrote and revised the manuscript. **Competing interests:** The authors declare that they have no competing interests. **Data and materials availability:** All data needed to evaluate the conclusions in the paper are present in the paper and/or the Supplementary Materials.

Submitted 29 March 2021
Accepted 29 June 2021
Published 18 August 2021
10.1126/sciadv.abi7498

Citation: Y. Zhang, Z. Huang, Z. Cai, Y. Ye, Z. Li, F. Qin, J. Xiao, D. Zhang, Q. Guo, Y. Song, J. Yang, Magnetic-actuated "capillary container" for versatile three-dimensional fluid interface manipulation. *Sci. Adv.* **7**, eabi7498 (2021).